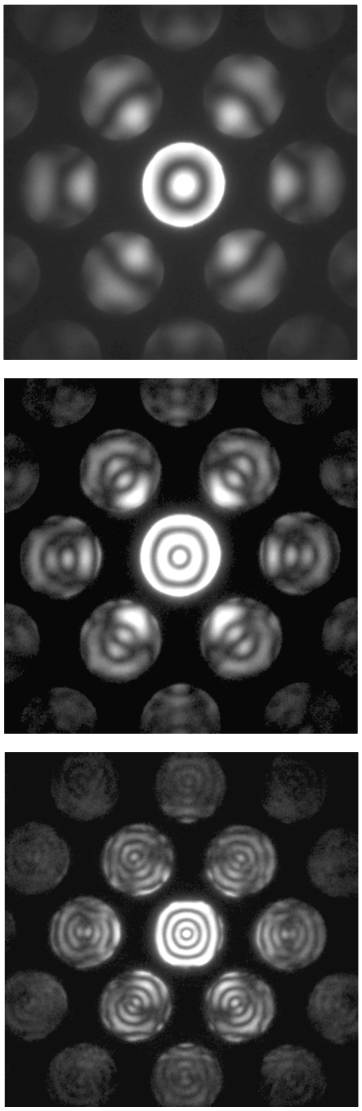

Figure 1. Energy-filtered CBED patterns recorded at 200kV at the <110> zone axis of Ni. The sample thickness increases from top to bottom. Note how the centre of the central disc remains bright at all thicknesses indicative of a critical voltage.

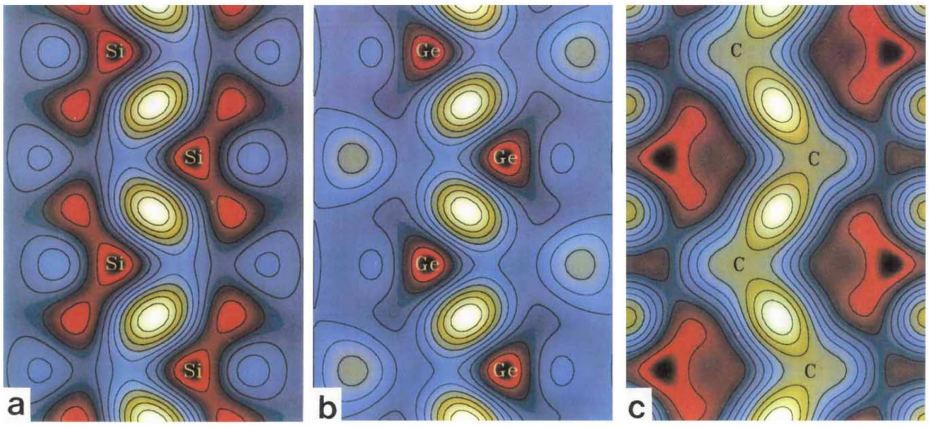

Figure 2. {110} slices of bond charge density for (a) silicon, (b) germanium, (c) diamond reconstructed from CBED pattern matching. The red/black regions indicate from where electron density has been moved into the yellow/white regions forming the atomic bond (taken from Saunders *et al*. 1996).

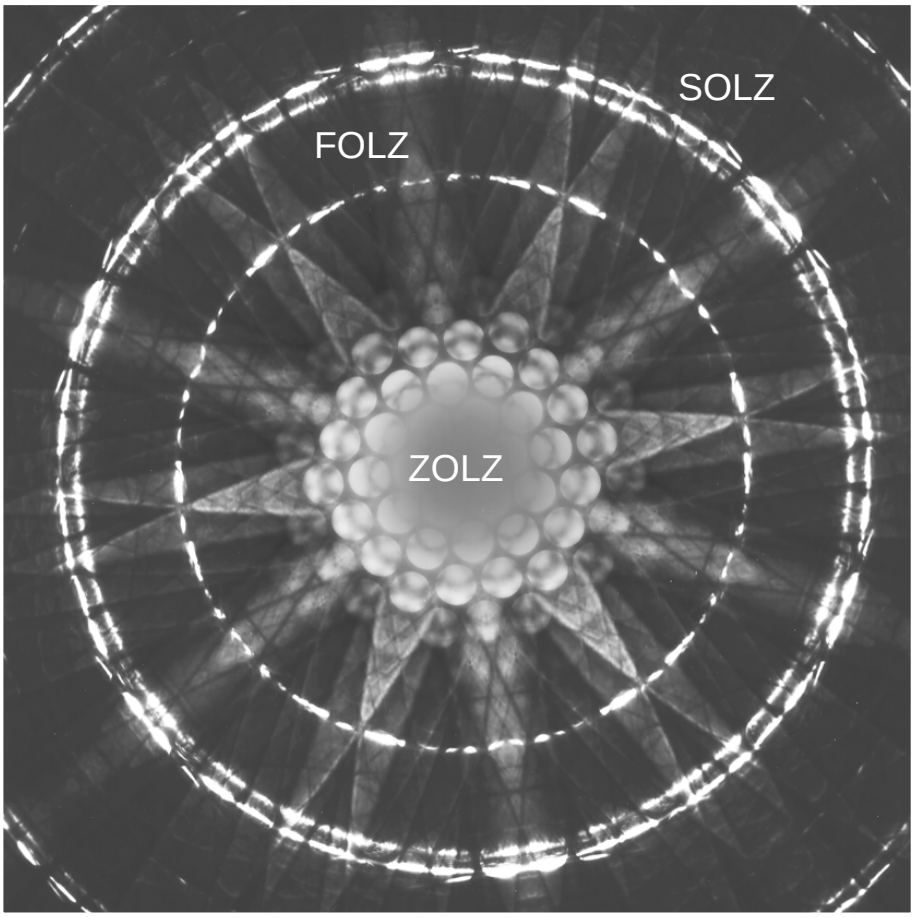

Figure 3. CBED pattern recorded from the [0001] axis of rhombohedral $LaAlO_3$. Odd HOLZ rings (e.g. FOLZ) show one branch arising from scattering from only oxygen atoms, even HOLZ rings (e.g. SOLZ) show two branches arising from scattering from separate strings of metal and oxygen atoms

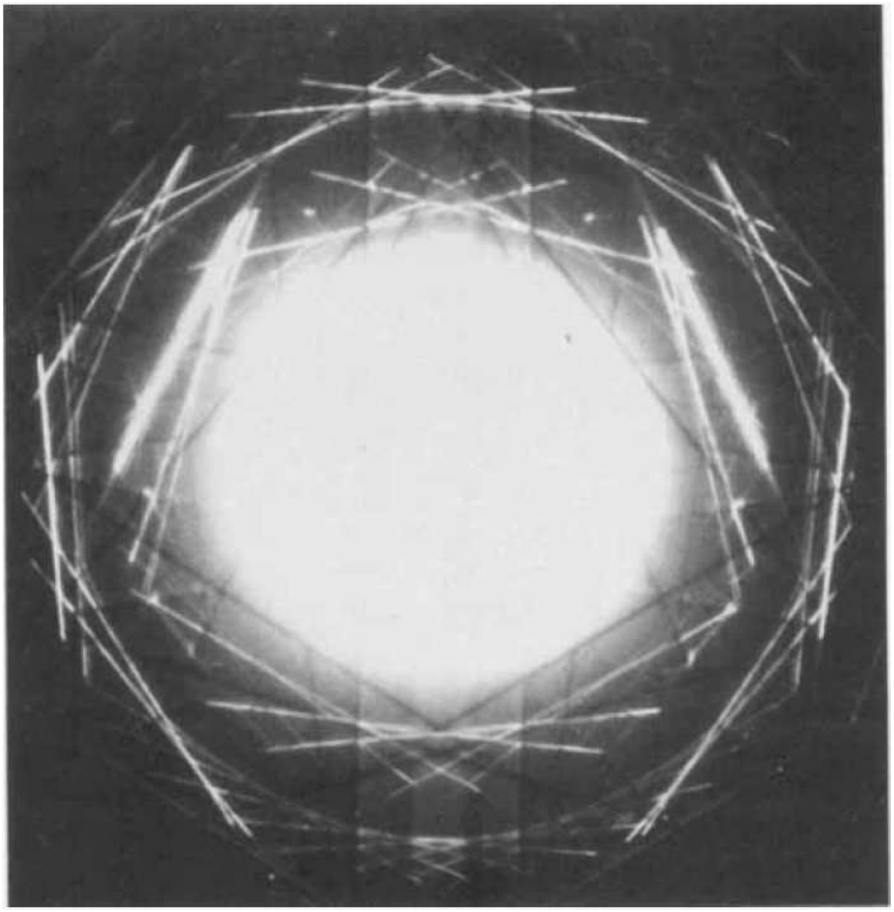

Figure 4. Focussed large-angle CBED pattern (‘Vincent pattern’) recorded from a metastable Al-Ge phase. Annuli of HOLZ reflections are evident which were used to solve the Al-Ge structure. Taken from Vincent and Exelby, 1993.

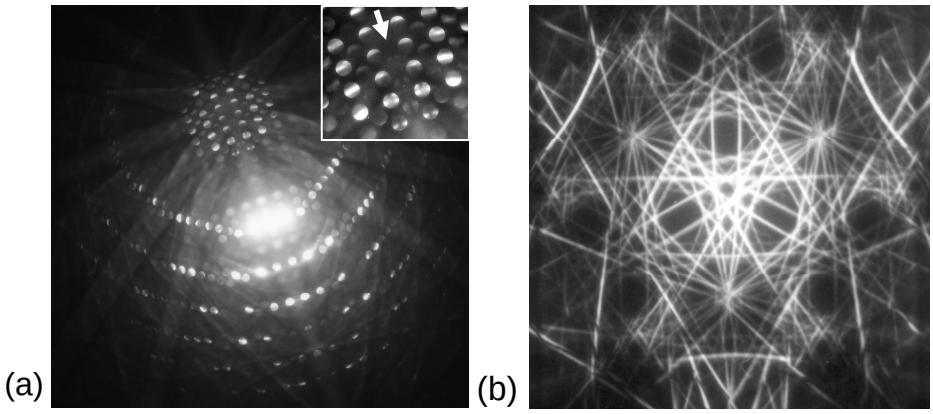

Figure 5. (a) An ‘inverse HOLZ’ pattern recorded from an unknown phase of $BiMnO_3$. The crystal is tilted such that the Ewald sphere intercepts reflections in the ‘negative’ FOLZ layer close to their Bragg condition. This enables detail within the FOLZ discs to be clearly seen, such as the Gjonnes-Moodie lines, indicative of a glide plane in this case, arrowed in the inset. (b) By setting up a hollow-cone illumination whose cone angle is equal to the FOLZ radius, it is possible to visualise a net of FOLZ reflections at the centre of such a hollow cone pattern. In this case we see the FOLZ reflections at a Si <111> zone axis.

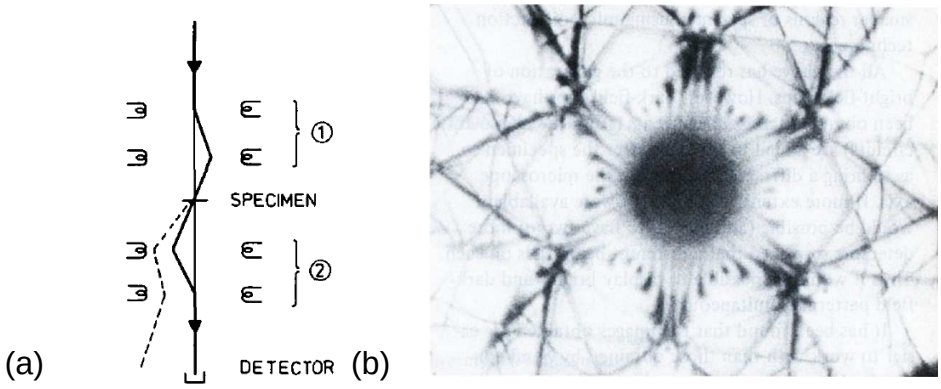

Figure 6. (a) A schematic of the double-rocking system proposed by Eades. The upper coils enable an angular raster of the beam on the sample, the lower coils compensate for the beam tilt to bring the beam back on axis. A STEM BF detector is sued to acquire the beam intensity (b) An Eades double-rocked pattern recorded from the <111> axis of Si. Taken from Eades, 1980.

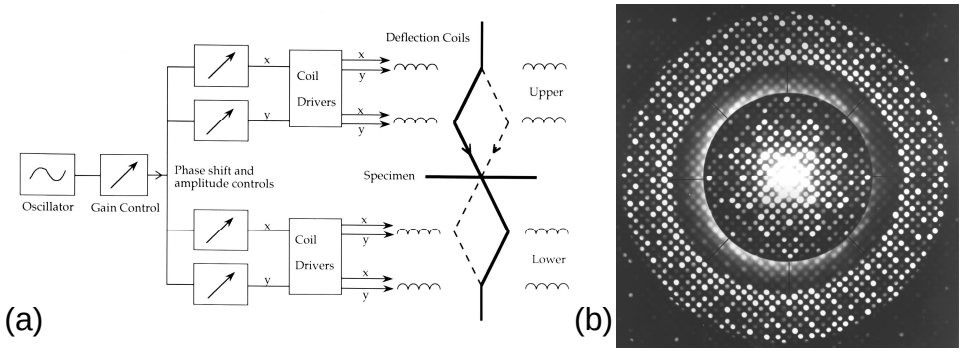

Figure 7. (a) A block diagram of the double-conical rocking system to acquire precession electron diffraction patterns such as the one shown in (b) recorded from the [001 zone axis of $Er_2Ge_2O_7$. Taken from Vincent and Midgley, 1994.

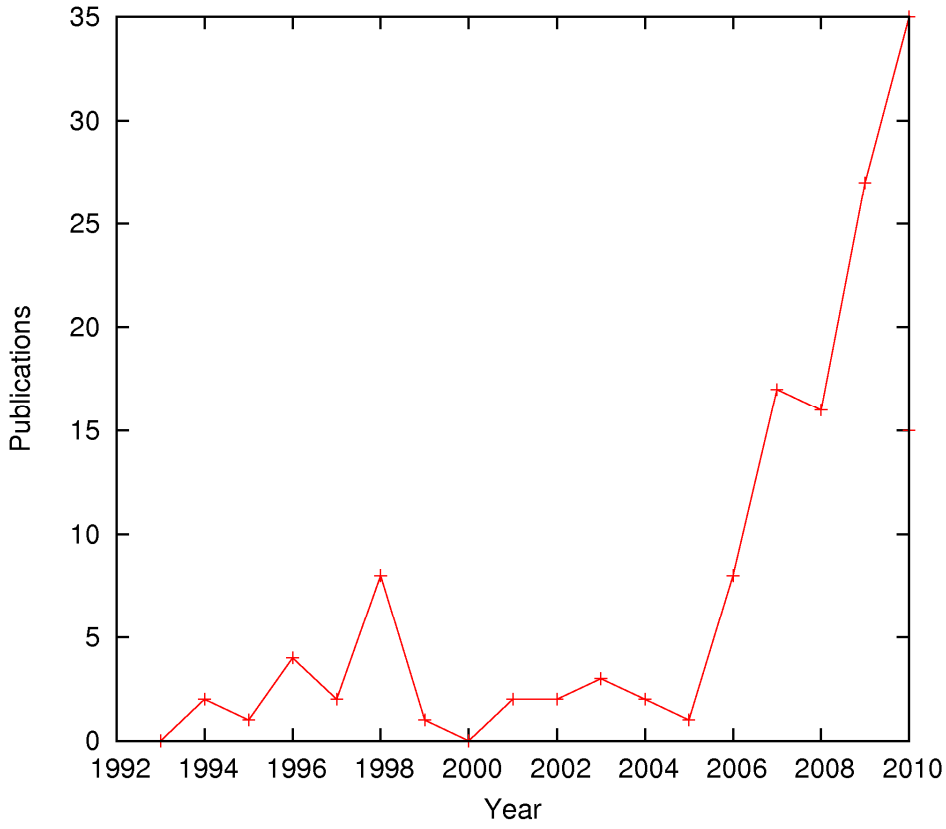

Figure 8. The number of published articles relating to PED as a function of publication year. The popularity of the technique has increased greatly since precession apparatus has become commercially available.

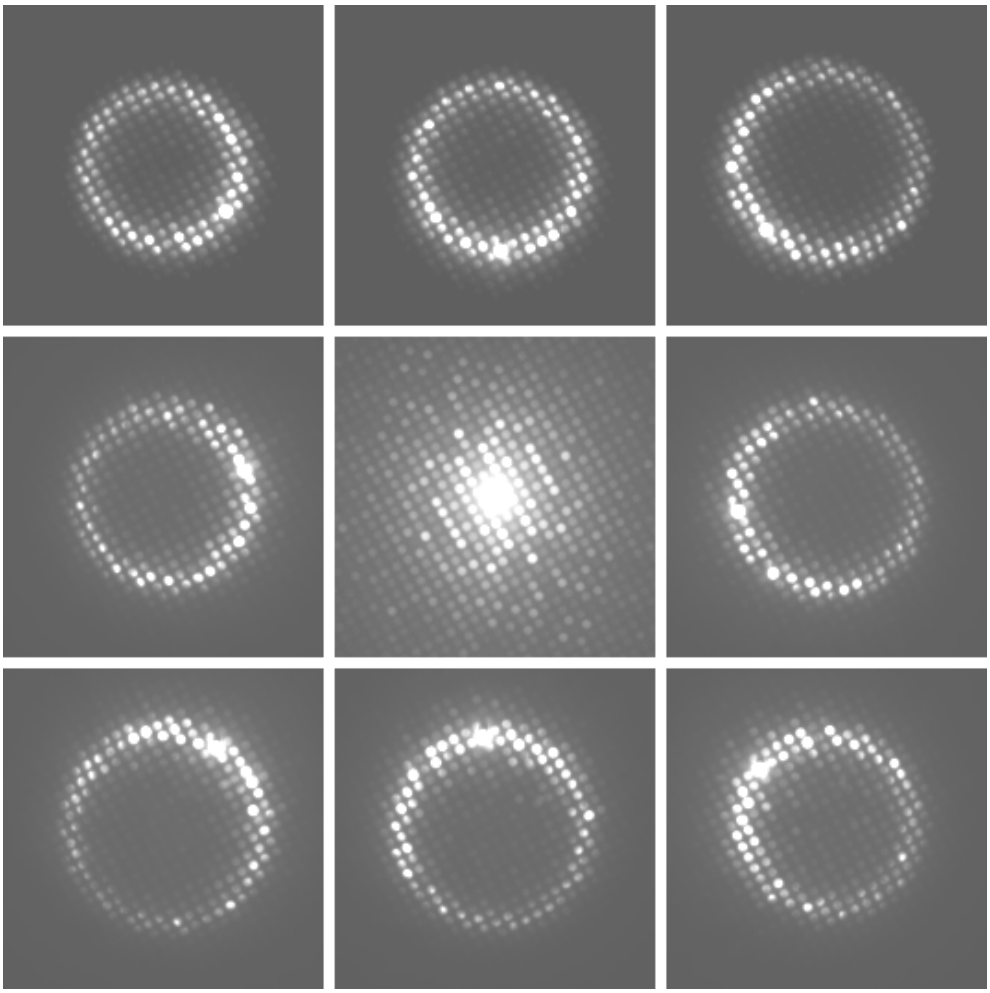

Figure 9. Diffraction patterns recorded from a sample of bismuth manganite, patterns are recorded at several point around a precession circle of approximately 1.5^{o} tilt. The diameter of the Laue circle is twice the applied precession angle. The full PED pattern is shown in the centre.

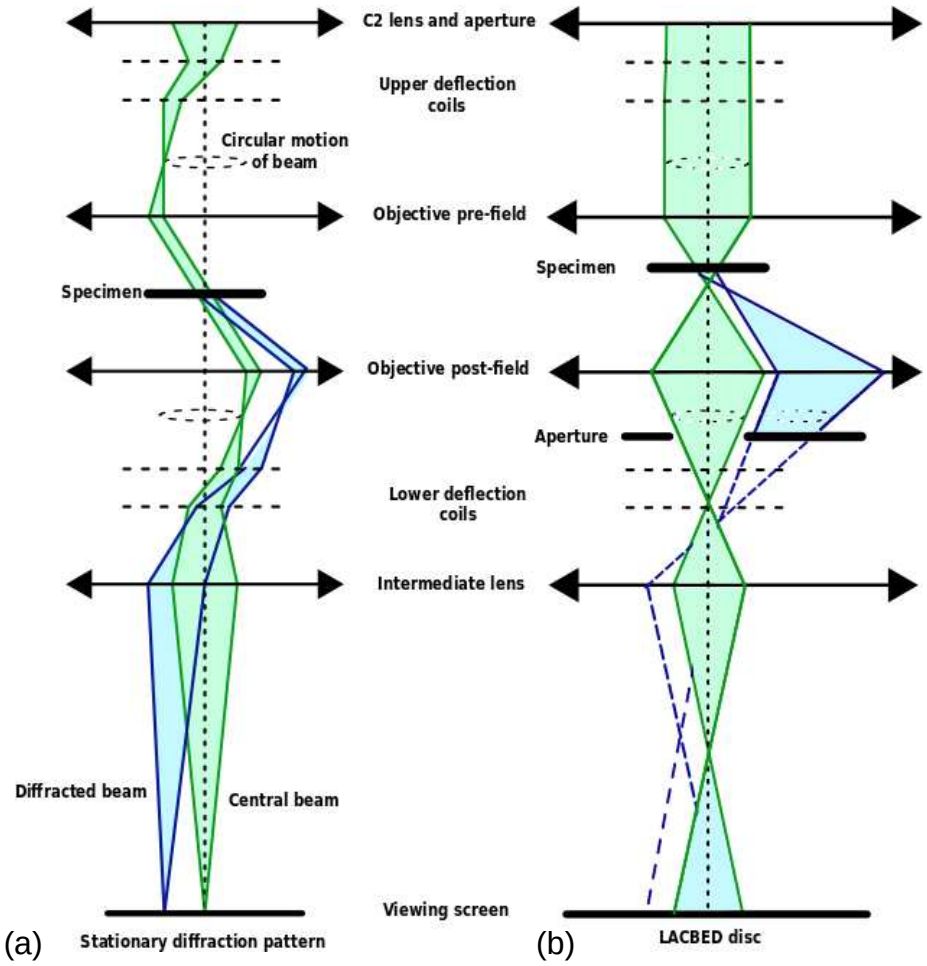

Figure 10. A comparative ray diagram of (a) precession electron diffraction showing the central beam and one diffracted beam; and (b) LACBED showing the central BF disc and one diffracted beam stopped by the SA aperture. Taken from Eggeman *et. al.* 2010.

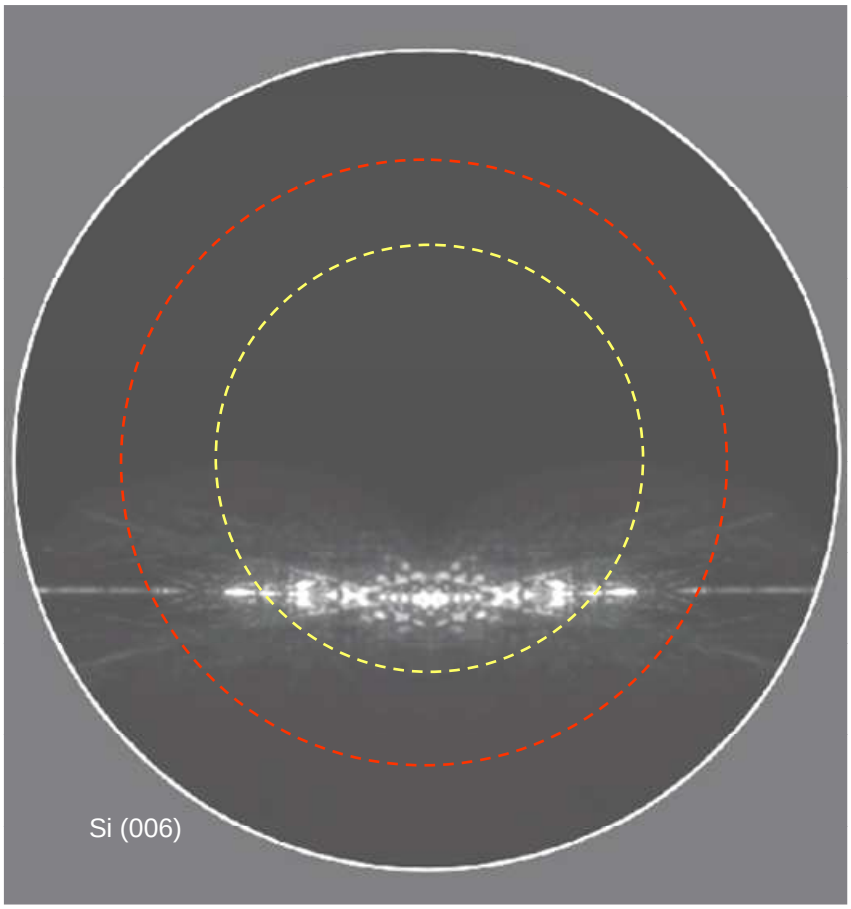

Figure 11. DF 006 LACBED from Si with the integration paths of two prececssion angles shown. The larger (red) path will yield precessed intensities with less multi-beam dynamical perturbation.

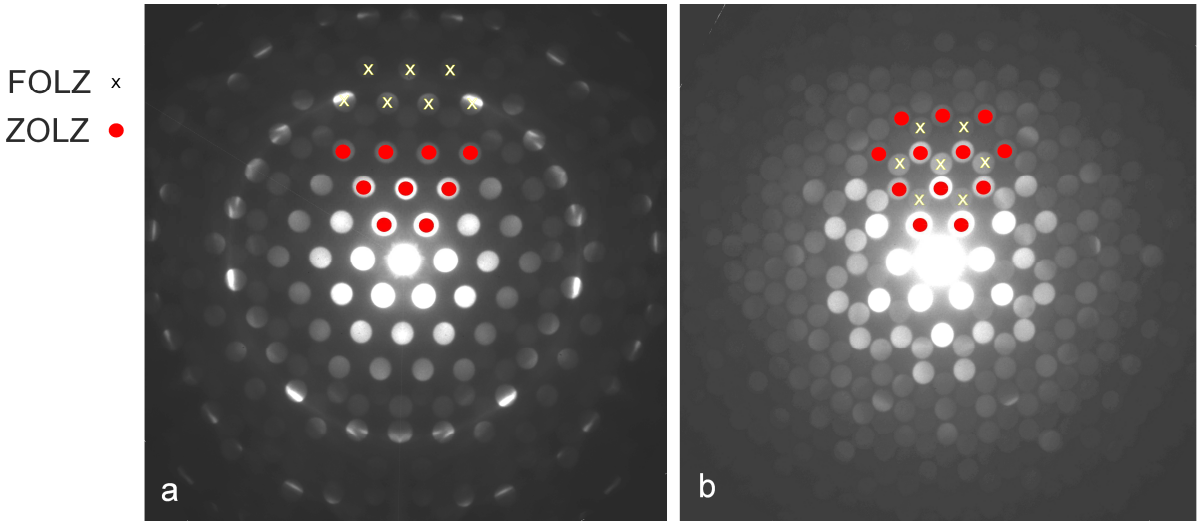

Figure 12 diffraction patterns from orthorhombic bismuth manganite with a) 0 mrad and b) ~20 mrad precession applied. ZOLZ reflections are labelled with a red circle, FOLZ reflections with a plain ‘X’. ‘HOLZ creep’ is mitigated by the non-overlapping reflections in different Laue Zones.

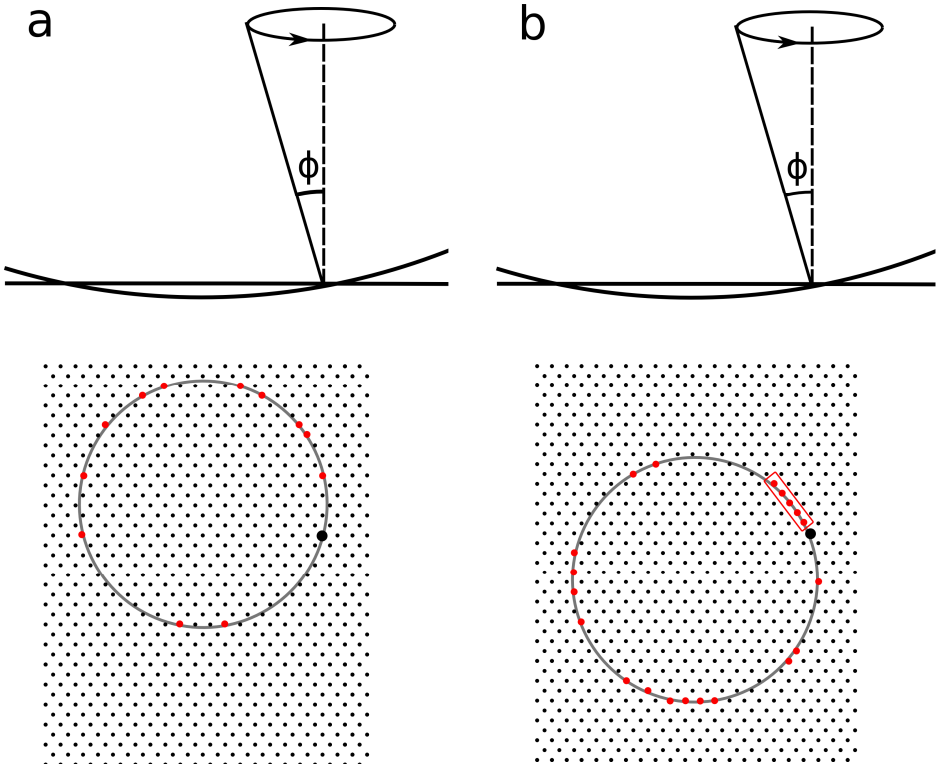

Figure 13. Schematic diagram of the onset of systematic row excitation with precession angle. Different azimuthal angles give rise to a) a Laue circle of excited reflections, b) systematic row excitation (indicated) in the Laue circle. Adapted from Mornirolo and Ji 2009

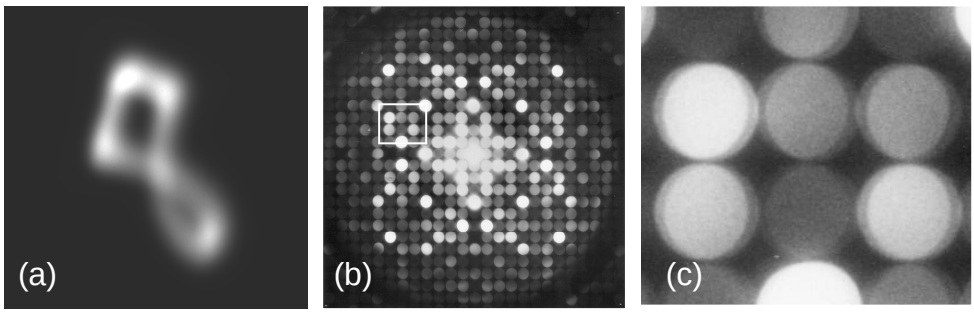

Figure 14 (a) A typical ‘knot’ of beam intensity seen on the specimen for a precessed focussed beam. The ‘knot’ comes about through driving the tilt coil electronics beyond their specification. (b) and (c) Evidence of imperfect descanning – the lower coils are not balancing the upper coils and the CBED discs are not perfectly overlapped. Taken from Sleight 1997.

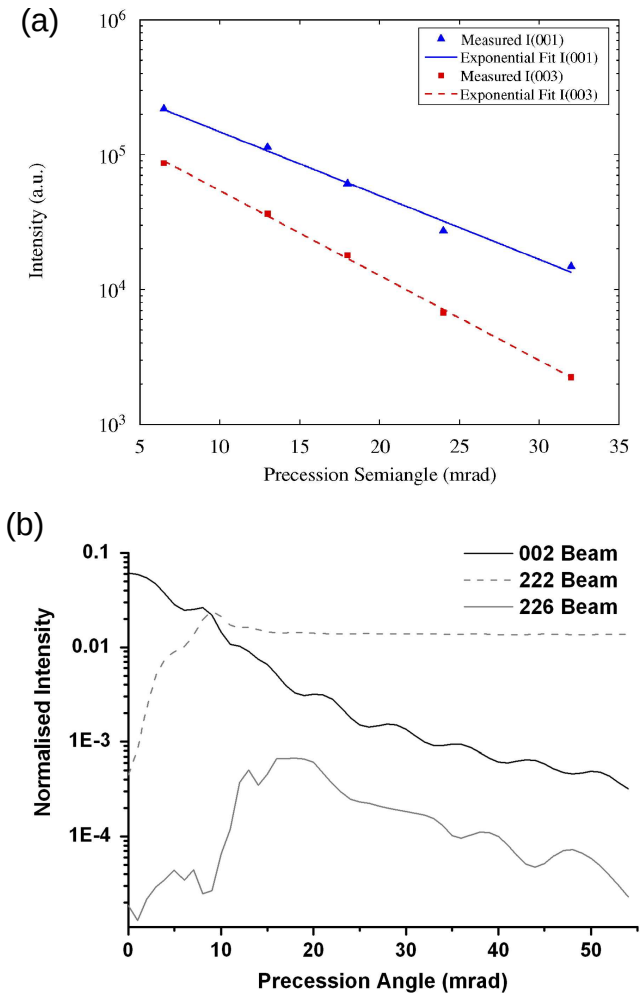

Figure 15 (a) Plot of the intensity of the kinematically forbidden (001) and (003) reflections in andalusite as a function of precession angle (taken from Ciston *et. al.* 2008). (b) simluated intensity of kinematically forbidden reflections in silicon as a function of precession angle (taken from Eggeman *et. al.* 2010).

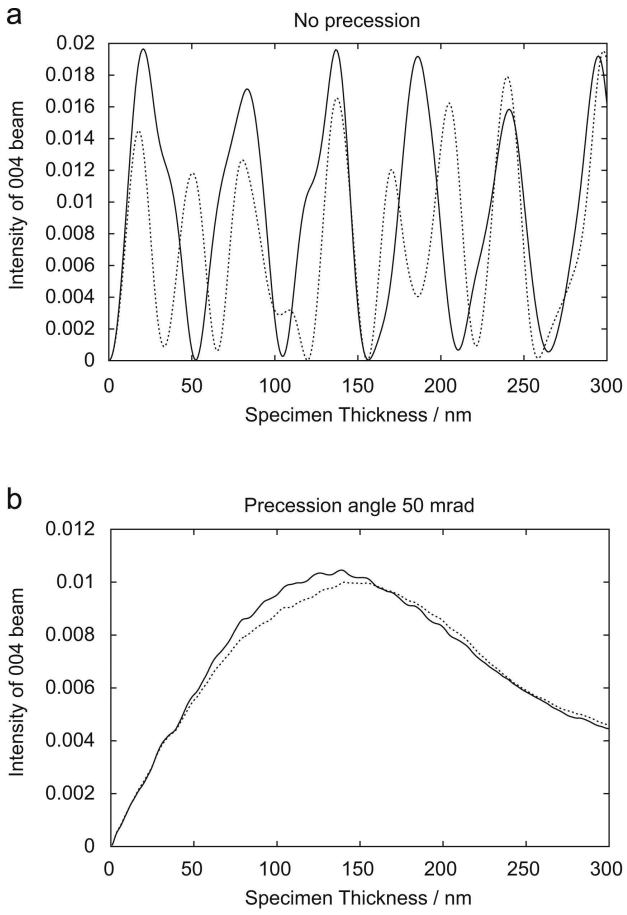

Figure 16. Comparison of the 004 intensity as function of sample thickness for silicon (solid line) and the 'randomised' structure (dotted line) with (a) 0 and (b) 50 mrad precession angle (taken from White *et. al.* 2010a).

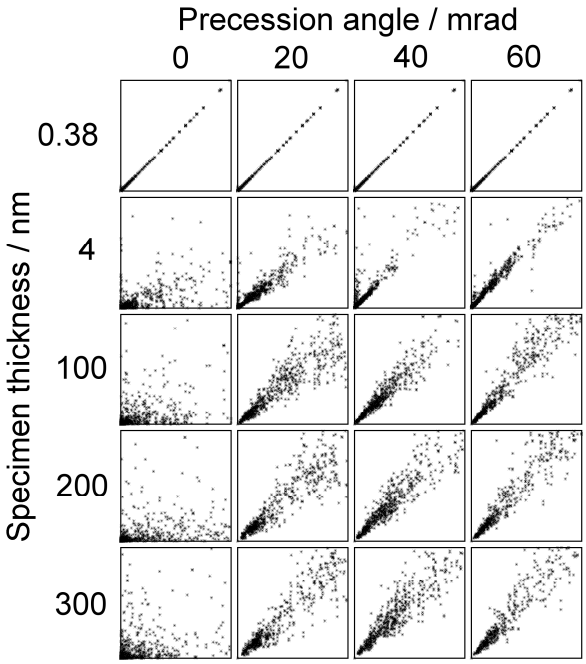

Figure 17. Correspondence plots between diffraction intensities from a silicon homometric pair, as a function of thickness and precession angle, with the most intense reflections shown nearest the origin of the plots. High correspondence is seen at large precession angles even for relatively thick samples. Taken from White *et. al*. 2010a.

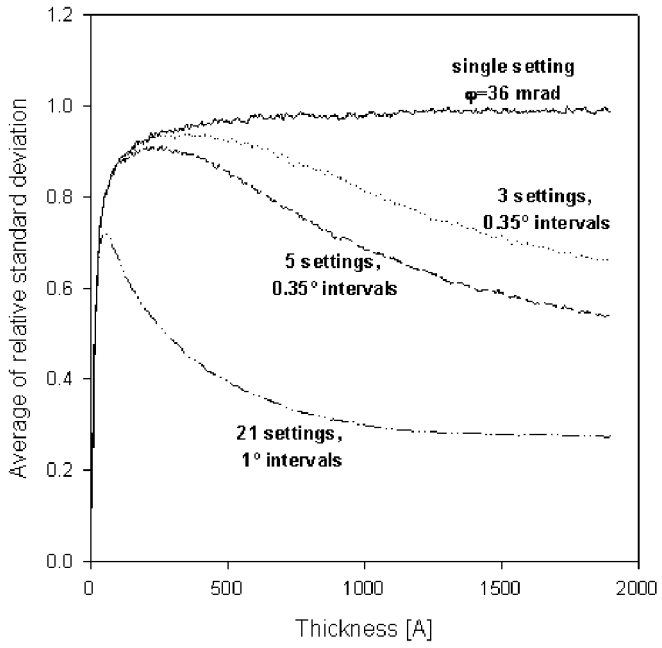

Figure 18. Average standard deviations of reflections as a function of crystal thickness. 50 sets of random phases were simulated and the intensities averaged over, the number and size of steps around the precession circle (precession angle is 36 mrad) included in the simulations are indicated. Taken from Sinkler & Marks 2010.

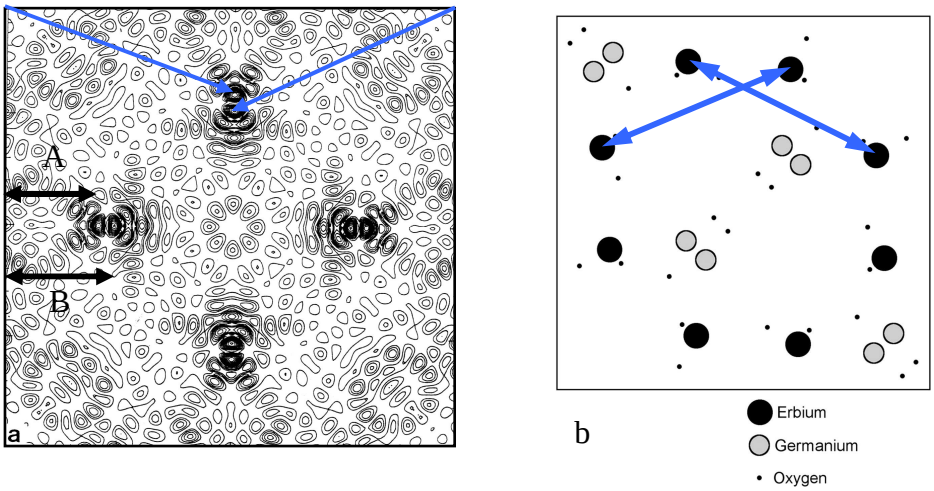

Figure 19. The modulus of the FOLZ conditional Patterson map calculated for the [001] FOLZ data seen in Figure 7b. The two peaks in the map correspond to Er-Er interatomic vectors seen in the $Er_2Ge_2O_7$ [001] projection in (b). Adapted from Vincent & Midgley, 1994.

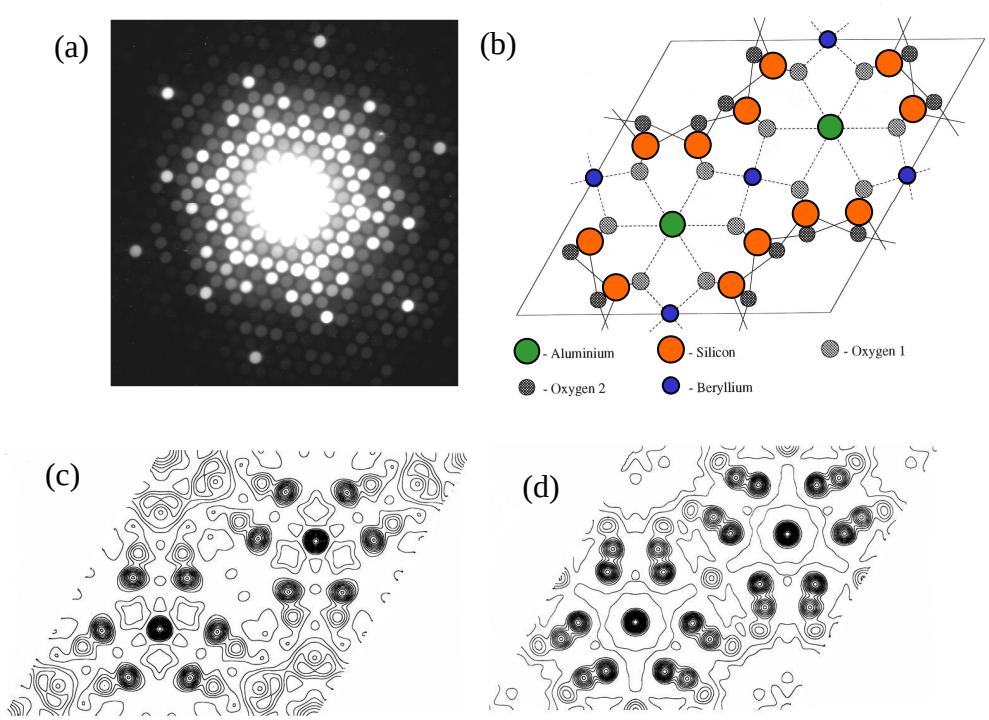

Figure 20. [0001] precession electron diffraction pattern from beryl. (b) The [0001] projected structure of beryl. (c) Calculated Fourier map using the experimental precession intensities in (a); and (d) the ideal beryl Fourier map using the same set of reflections. Figures adapted from Sleight 1997.

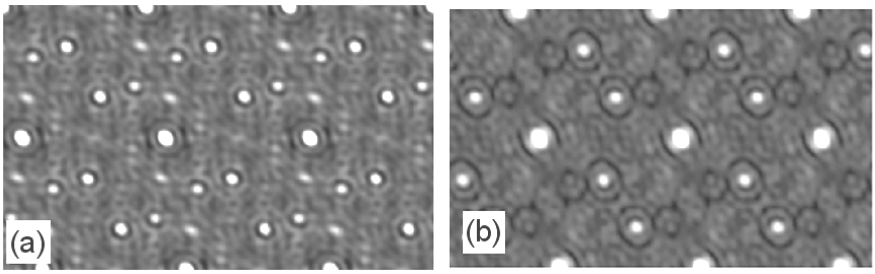

Figure 21. Structure solutions of the [010] projection of GITO produced from (a) precession electron diffraction intensities and (b) conventional electron diffraction intensities. Figures adapted from Own *et.al*. 2006a.

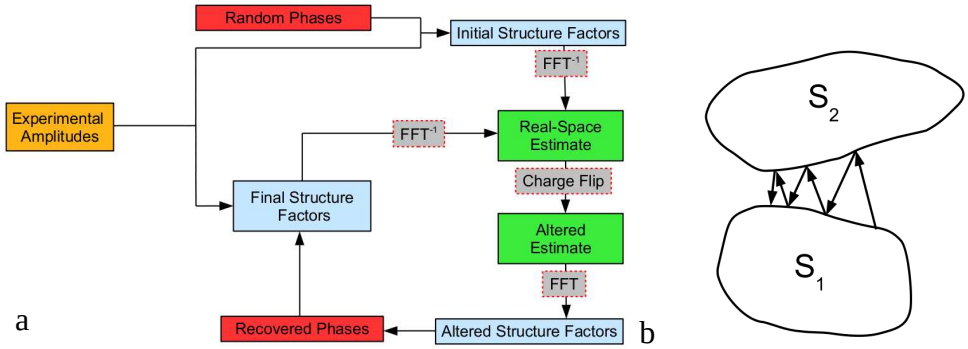

Figure 22. (a) Schematic diagram of a charge-flipping algorithm and (b) a representation of the evolution of charge-flipped solution. Taken from Eggeman *et al*. 2009.

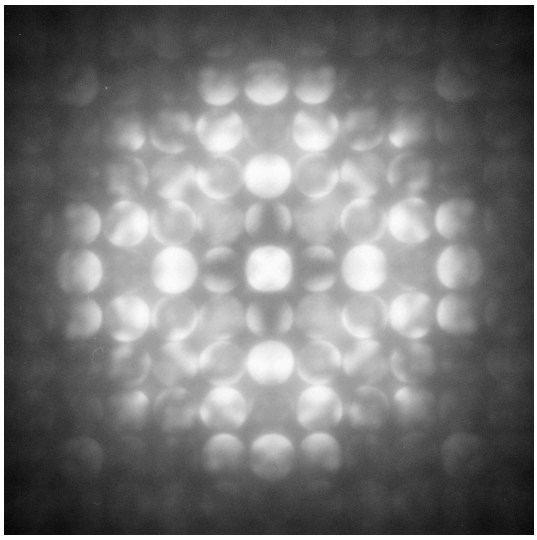

Figure 23.CBED ZOLZ pattern recorded parallel to [001] of erbium pyrogermanate. GM lines both horizontal and vertical together with rotational symmetry confirm the *p4gm* plane-group symmetry of this projection.

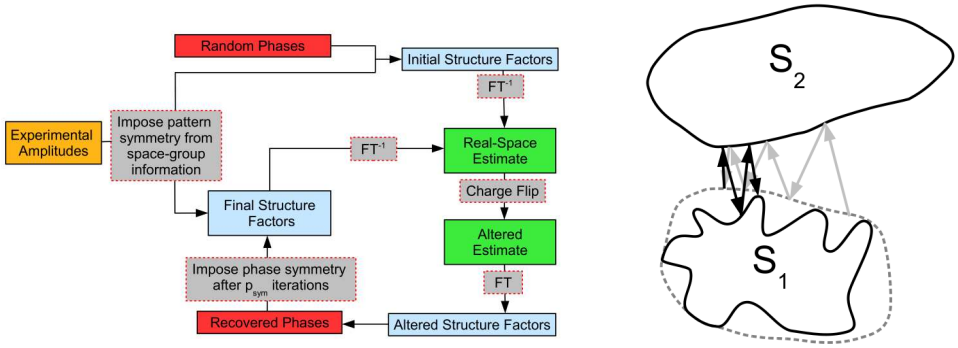

Figure 24. (a) Schematic diagram of the symmetry modified charge-flipping algorithm. (b) a representation of the evolution of charge-flipped solution after the introduction of projection symmetry into the algorithm. Taken from Eggeman *et al*. 2009.

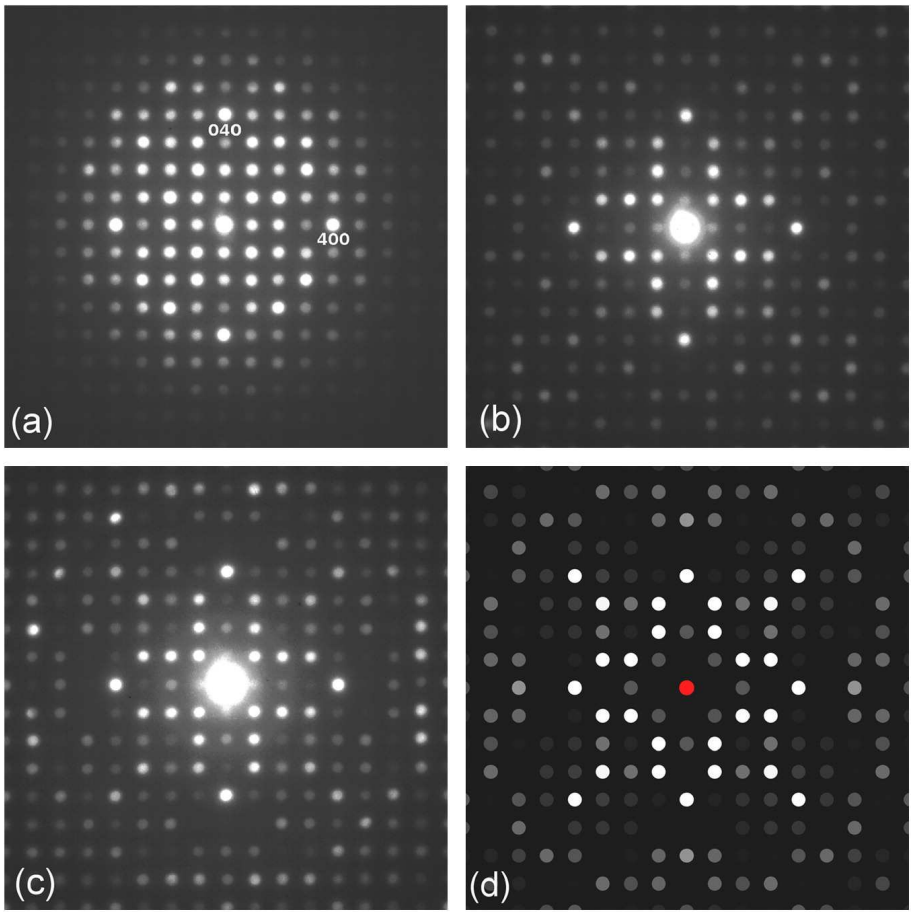

Figure 25. [001] electron diffraction patterns of $Er_2Ge_2O_7$ recorded at precession angles of (a) 0 mrad, (b) 20 mrad and (c) 47 mrad. A simulated kinematical diffraction pattern is shown in (d). Figures from Eggeman et. al. 2010.

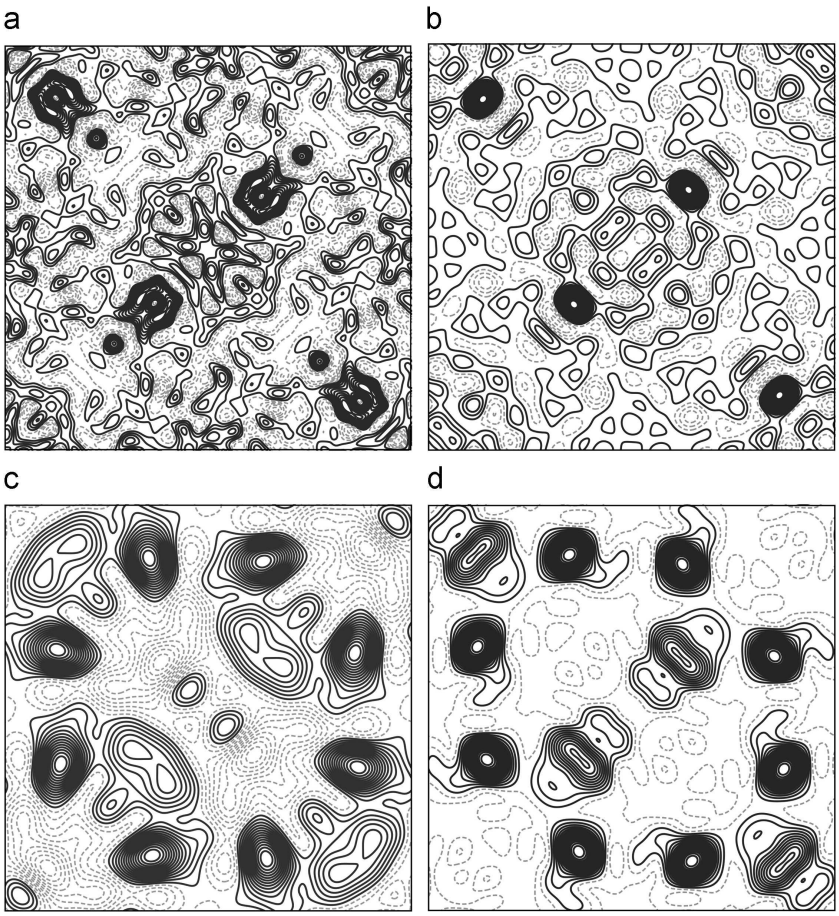

Figure 26. Structure solutions from [001] PED patterns of $Er_2Ge_2O_7$ recorded with precession angles of (a) 0 mrad (resolution of 0.349Å^{-1}), (b) 20mrad (0.499Å^{-1}) and (c) 47mrad (0.718 Å^{-1}). The kinematical ideal solution at a resolution of 0.718Å is included in (d) for comparison. Figures taken from Eggeman *et. al*. 2010.

(a)

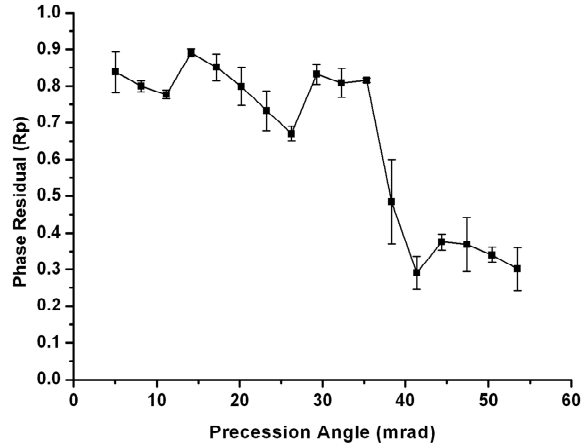

(b)

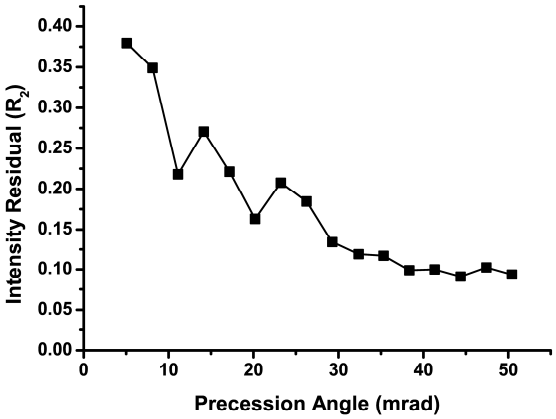

Figure 27. (a) Phase residual, R_p, calculated from the structure solutions for a series of precessed diffraction patterns recorded at the [001] zone axis of $Er_2Ge_2O_7$. The values are the mean residual for five solutions for the particular set of reflections, error bars indicate the range of R_p values. (b) Unweighted intensity residual R_2 calculated from precessed electron diffraction patterns – see text for details. Figures taken from Eggeman et. al. 2010.

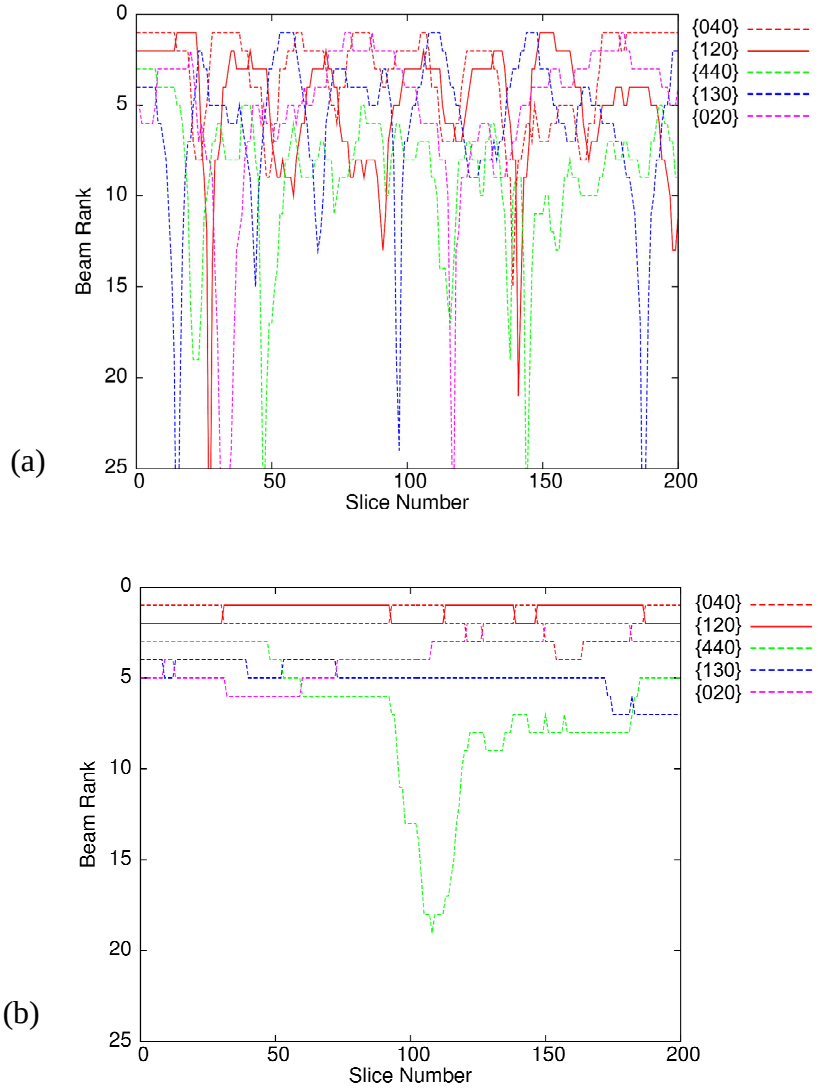

Figure 28. The relative order of the five kinematically strongest reflections in erbium pyrogermanate, as a function of thickness, with (a) zero and (b) 40 mrad precession angle. Adapted from Barnard et. al. 2009.

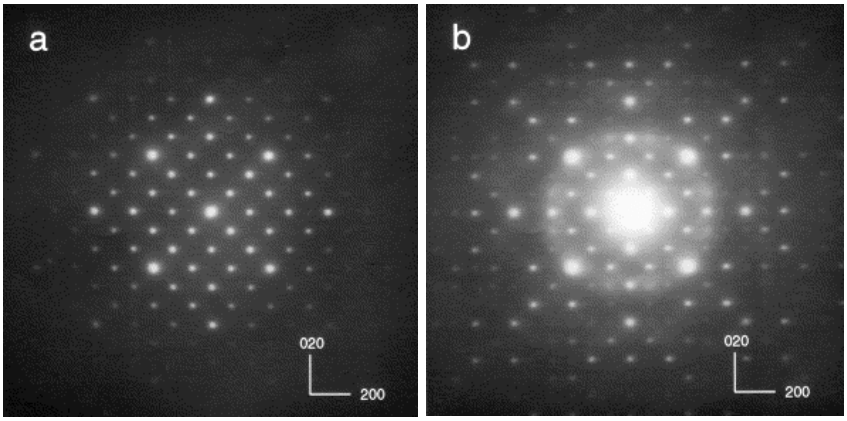

Figure 29. A comparison of [001] electron diffraction patterns from a tetragonal inter-metallic alloy phase Al_mFe. (a) SAD pattern, (b) precessed pattern with precession angle, $\phi = 2.35°$. Taken from Berg *et. al.* 1998.

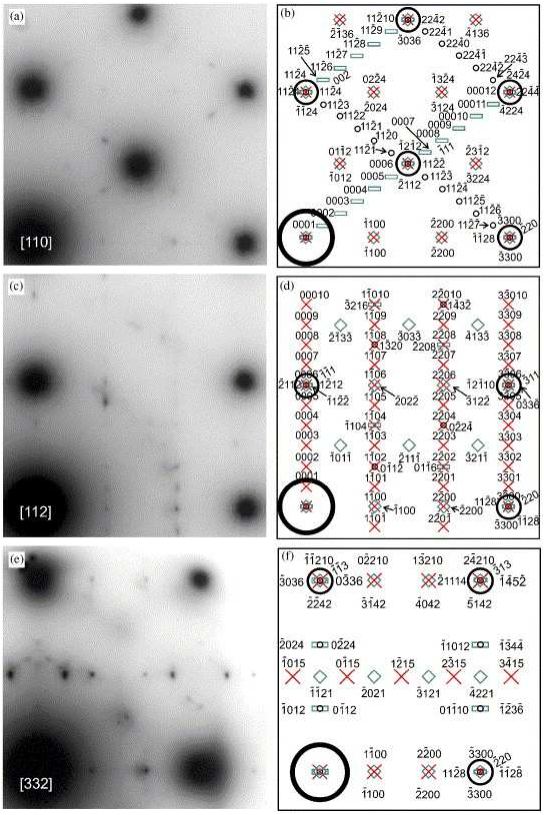

Equivalent orientation of planes and directions of η' relative to the aluminium matrix

Colour	Symbol	Orientation
Green	◇	$(0\,0\,0\,1)_{\eta'} \| (111)_{Al}$ and $[2\,\bar{1}\,\bar{1}\,0]_{\eta} \| [\bar{1}\,\bar{1}\,2]_{Al}$
Blue	▭	$(0\,0\,0\,1)_{\eta} \| (\bar{1}\,1\,1)_{Al}$ and $[2\,\bar{1}\,\bar{1}\,0]_{\eta} \| [1\,\bar{1}\,2]_{Al}$
Red	×	$(0\,0\,0\,1)_{\eta} \| (\bar{1}\,\bar{1}\,1)_{Al}$ and $[2\,\bar{1}\,\bar{1}\,0]_{\eta} \| [1\,1\,2]_{Al}$
Black	○	$(0\,0\,0\,1)_{\eta} \| (1\,\bar{1}\,1)_{Al}$ and $[2\,\bar{1}\,\bar{1}\,0]_{\eta} \| [\bar{1}\,1\,2]_{Al}$

Figure 30. Precession diffraction patterns of Al-Zn-Mg precipitates along the Al [110] zone axis in (a), [112] in (c) and [332] in (e) with corresponding indexing in (b), (d) and (f), respectively. The table explains the symbols used to index the patterns and the orientation of the precipitate phase with respect to the matrix (taken from Kverneland *et. al.* 2006).

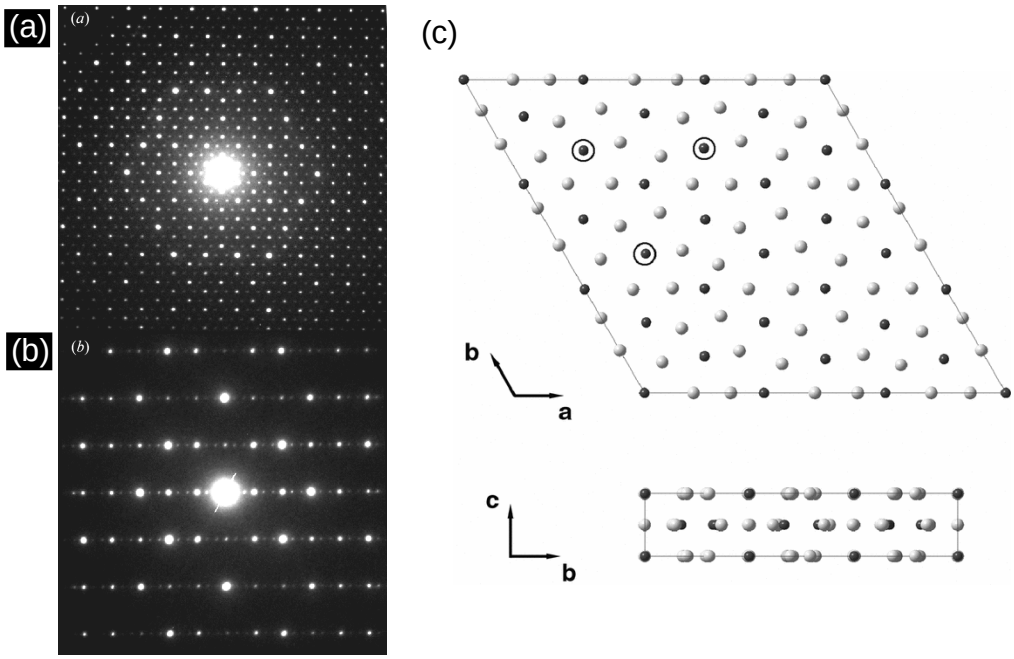

Figure 31. Precession patterns of Ti_2P from (a) [001] and (b) [010] zone axis. Note the mix of strong and weak reflections parallel to (*h*00) and (*hh*0) indicating superstructures (c) Proposed structure solution, ringed atoms indicate likely P vacancies (taken from Gemmi *et. al.* 2002).

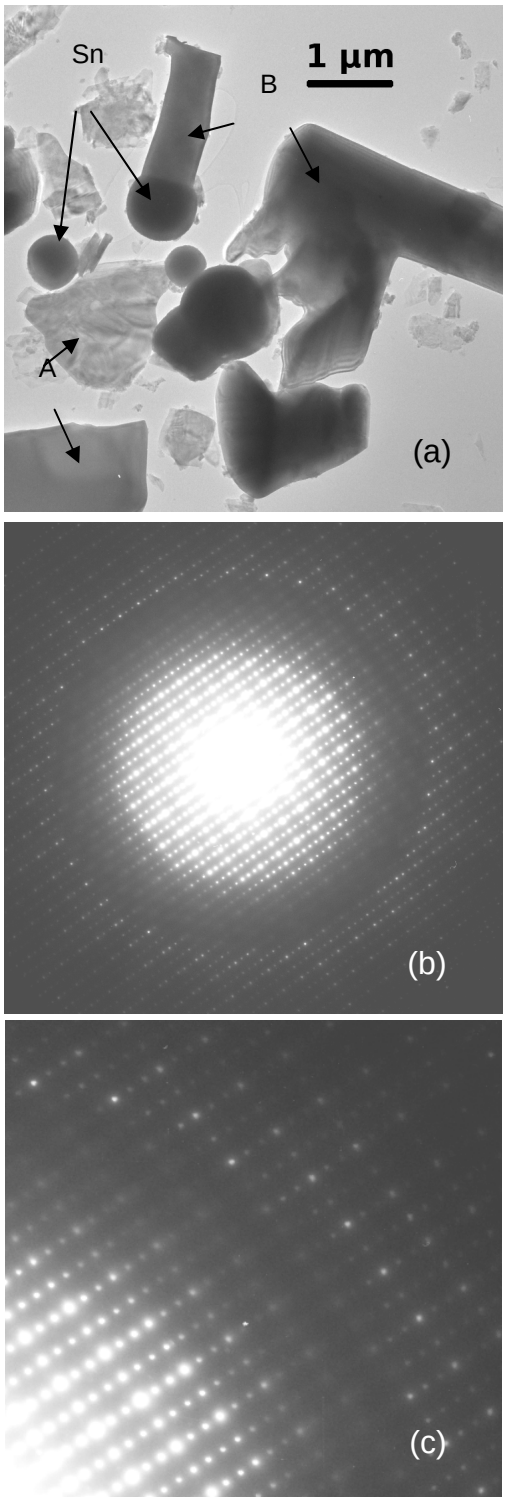

Figure 32. (a) micrograph showing primary tin particles and SnO_2 (denoted A) and the intermediate tin oxide phase growing from these (B). (b) [001] zone axis precession diffraction pattern and (c) detail from this pattern. Taken from White *et al*. 2010b.

(a) 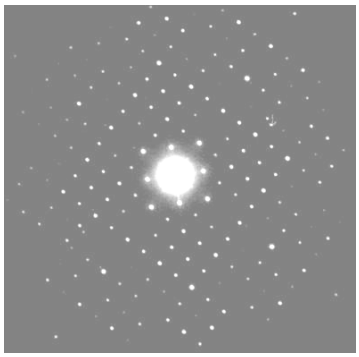 (b) 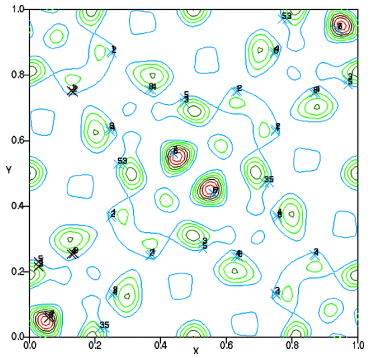

Figure 33. (a) [001] zone-axis precession diffraction pattern from MCM68 and (b) the resulting structure solved from the diffraction pattern. Taken from Dorset *et. al*. 2007.

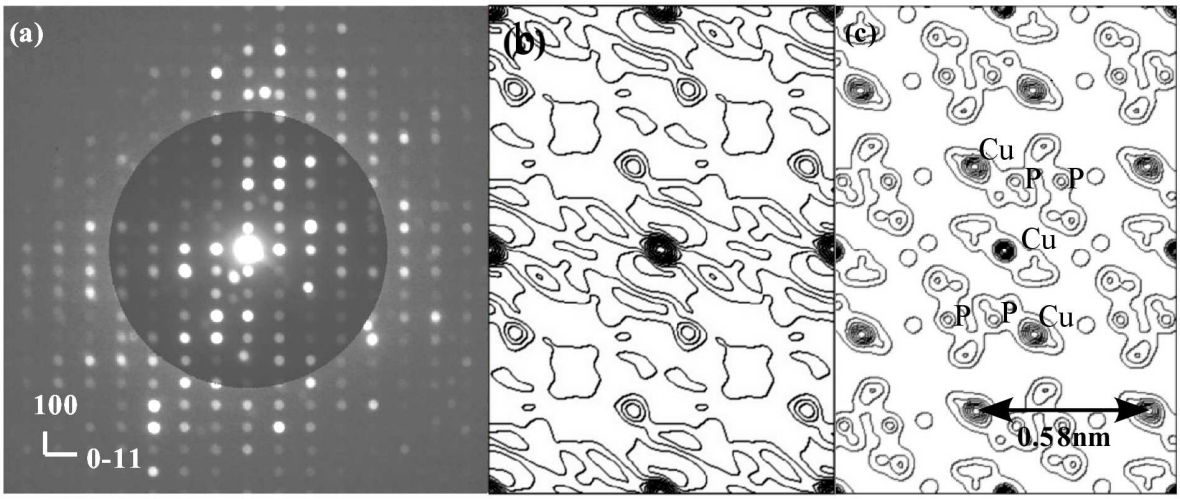

Figure 34 a) Experimental PED pattern recorded parallel to the [011] zone-axis of copper phosphonoacetate. b) potential map recovered from the experimental diffraction intensities and c) the potential map of the ideal structure with the heavy atoms sites labelled. Adapted from Bithell *et al*. 2010.

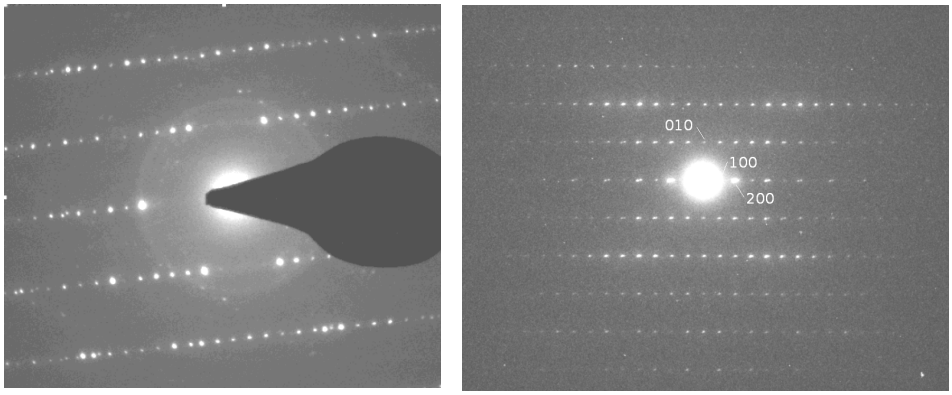

Figure 35. Precession electron diffraction patterns from (a) aspirin, taken from Nicolopoulis 2007, and (b) sildenafil citrate.

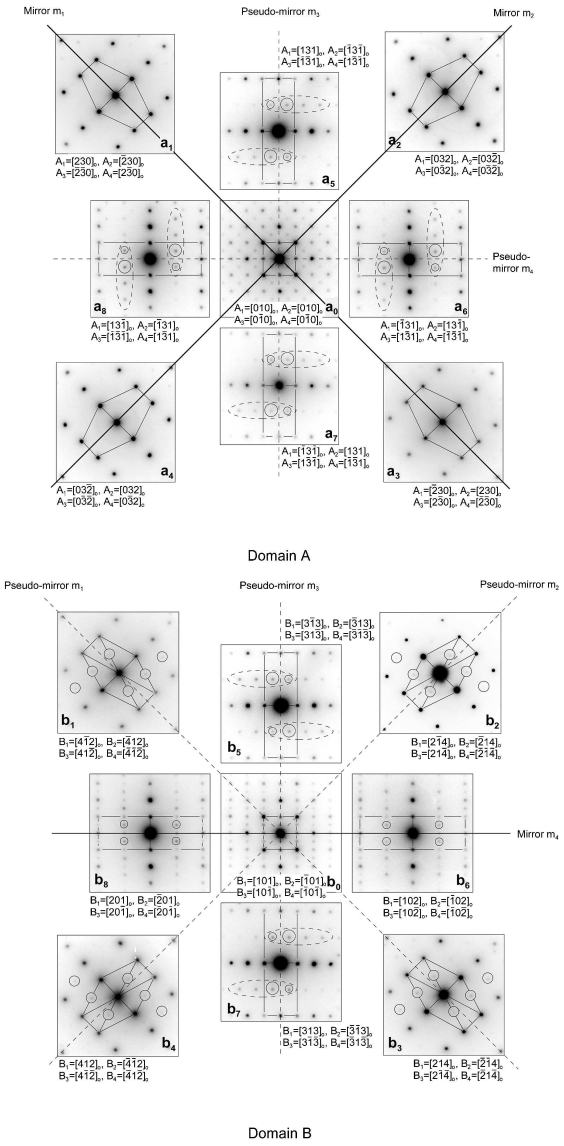

Figure 36. Sets of precession patterns taken from domains of twinned $LaGaO_3$. The patterns from domain A are located around the<010> zone axis and from B around the <101> zone axis, along mirrors and pseudo-mirrors. Four equivalent indices (A_1–A_4 and B_1–B_4) are given for each of the patterns. Taken from Ji *et. al.* 2009.

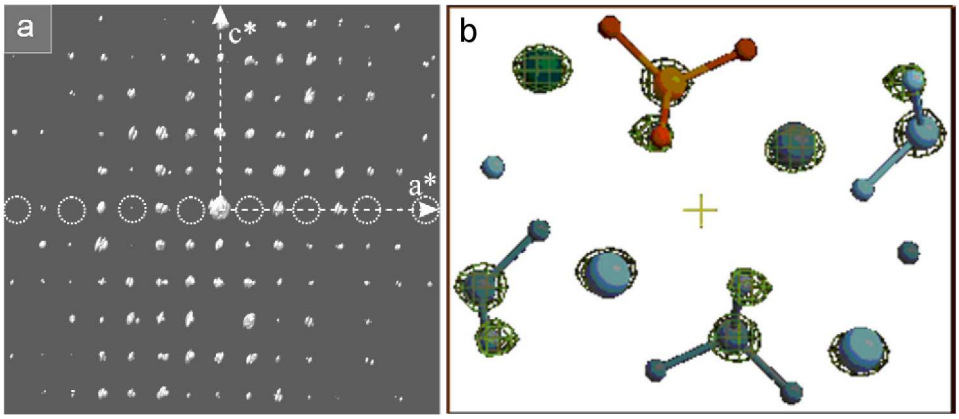

Figure 37. a) Reciprocal space wedge of $BaMnO_3$ reconstructed from a PED tilt series and shown projected along the [010]* direction, b) a structure solved from the experimental ADT data, the solid atoms are overlaid to indicate the correct atomic positions, in this structure the c-direction is horizontal and the a-direction is vertical. Taken from Mugnaioli *et al*. 2009

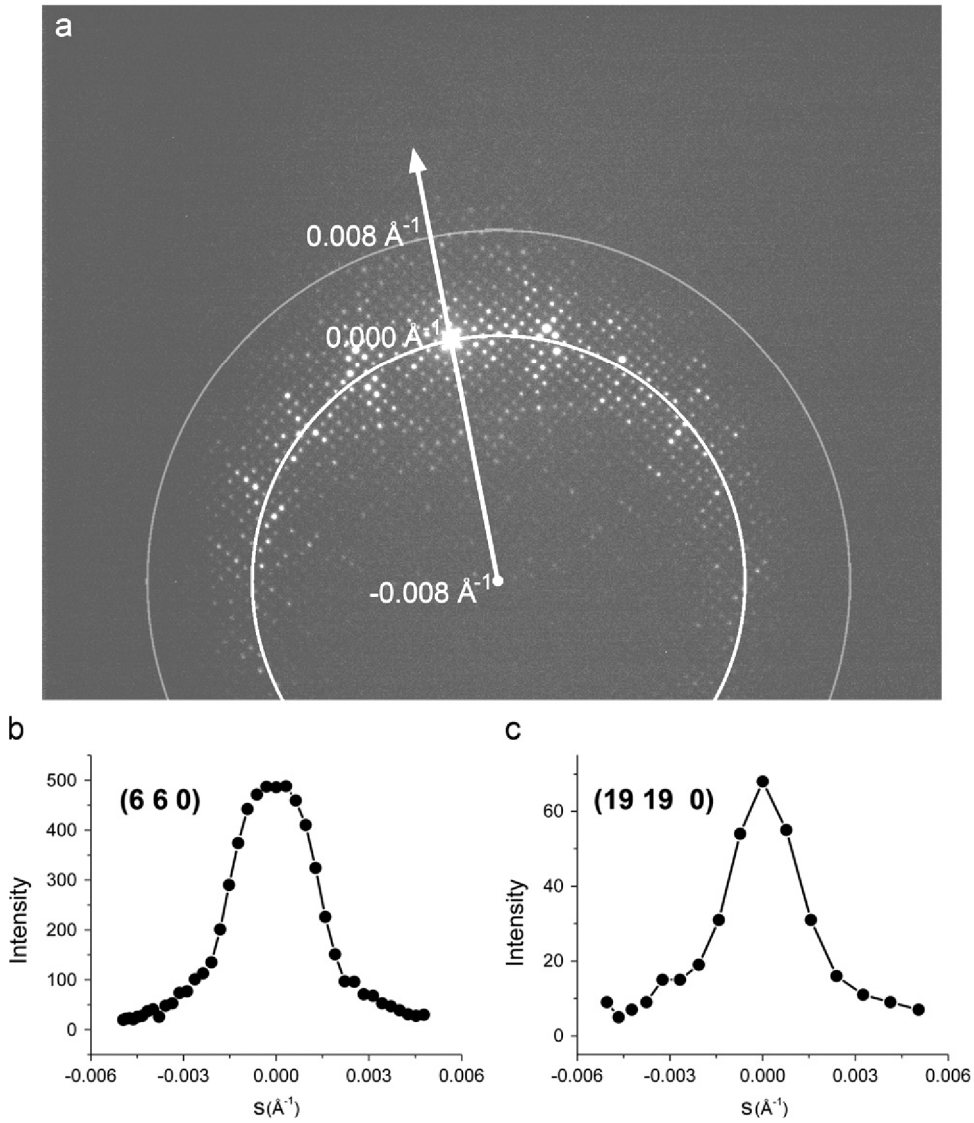

Figure 38. a) Sample diffraction pattern form a digitally sampled precession circle with experimentally recovered rocking curves for b) (6 6 0) and c) (19 19 0) reflections. Taken from Zhang *et al*. 2010b

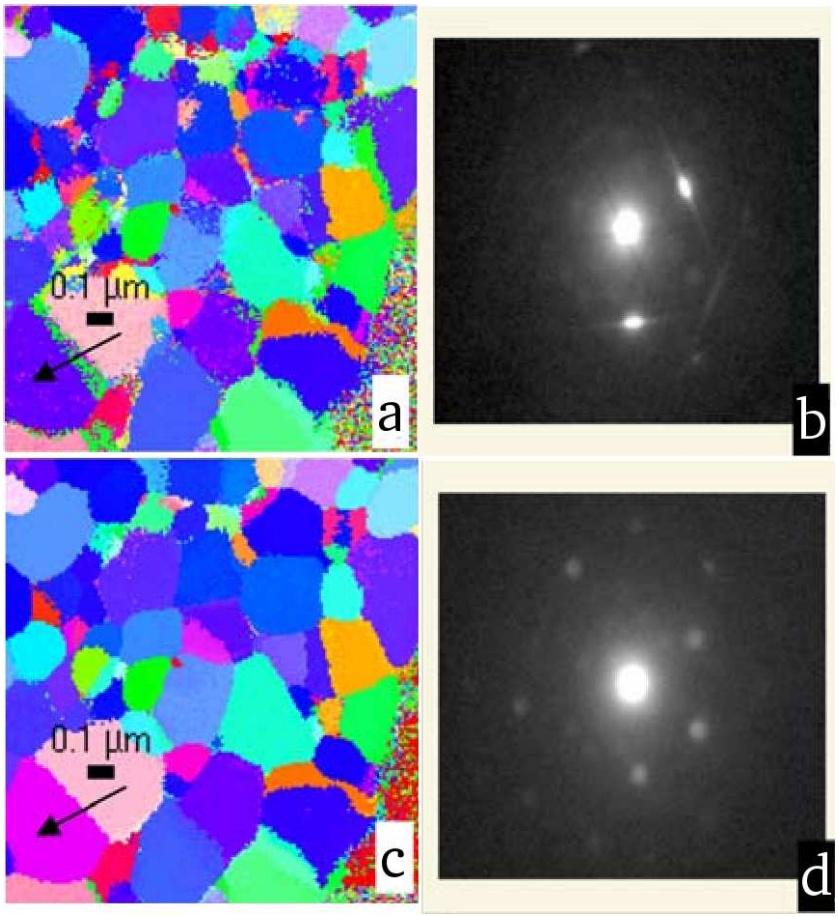

Figure 39. Orientation maps and typical diffraction patterns recorded using no precession (a and b respectively) and those recorded using ~0.9^{o} precession (c and d respectively). Taken from Moeck *et al*. 2011

1	Finite Kinematical	Geometry Only	$C_{kin}(g,t,\phi) = \left(\frac{1}{\xi_g^2} \int_0^{2\pi} \frac{\sin^2 \pi t s_g(\theta)}{s_g{}^2(\theta)} d\theta \right)^{-1}$
2	Finite Dynamical	Full Correction	$C_{2beam}(g,t,\phi) = \left(\frac{1}{\xi_g^2} \int_0^{2\pi} \frac{\sin^2 \pi t s_g^{eff}}{(s_g^{eff})^2} d\theta \right)^{-1}$
3	Gjønnes	Geometry Only	$C_{Gj}(g,\phi) = g\sqrt{1-\left(\frac{g}{2R_0}\right)^2}$
4	Gjønnes–Blackman	Full Correction	$C_{Blackman}(g,t,\phi) = g\sqrt{1-\left(\frac{g}{2R_0}\right)^2} \cdot \frac{A_g}{\int_0^{A_g} J_0(2R)dx}$

Table 1. Correction (Lorentz) factors for precession electron diffraction intensities. Note that θ is the azimuthal angle around the precession circle, $s_g(\theta) = \frac{g^2 - 2k\phi g\cos\theta}{2k}$ and $s_g^{eff} = \sqrt{s_g^2 - \frac{1}{\xi_g^2}}$. Adapted from Own 2005.